A 1.2-V 5.2-mW 20–30-GHz Wideband Receiver Front-End in 0.18-μm CMOS

Chun-Hsing Li, *Student Member, IEEE*, Chien-Nan Kuo, *Member, IEEE*, and Ming-Ching Kuo, *Member, IEEE*

***Abstract*—This paper presents a low-power wideband receiver front-end design using a resonator coupling technique. Inductively coupled resonators, composed of an on-chip transformer and parasitic capacitances from a low-noise amplifier, a mixer, and the transformer itself, not only provide wideband signal transfer, but also realize wideband high-to-low impedance transformation. The coupled resonators also function as a wideband balun to give single-to-differential conversion. Analytic expressions for the coupled resonators with asymmetric loads are presented for design guidelines. The proposed receiver front-end only needs a few passive components so that gain degradation caused by the passive loss is minimized. Hence, power consumption and chip area can be greatly reduced. The chip is implemented in 0.18-μm CMOS technology. The experimental result shows that the -3-dB bandwidth can span from 20 to 30 GHz with a peak conversion gain of 18.7 dB. The measured input return loss and third-order intercept point are better than 16.7 dB and -7.6 dBm, respectively, over the bandwidth. The minimum noise figure is 7.1 dB. The power consumption is only 5.2 mW from a 1.2-V supply. The chip area is only 0.18 mm^2.**

***Index Terms*—CMOS, common-gate (CG) low-noise amplifier (LNA), inductively coupled resonators (ICRs), low power, low voltage, mixer, resonator coupling network (RCN), wideband.**

I. Introduction

THE applications within the K- and Ka-band have ignited intensive research activities. There exist systems of 22–29-GHz short-range radar, 24-GHz industrial–scientific–medical (ISM) band, and local multipoint distribution services (LMDS) [1]–[4]. A wideband receiver is thus preferable to a narrowband one for versatile functions. However, designing a receiver to cover such a wide and high frequency band is challenging because of lossy passive components and low transistor speed. For example, 0.18-μm CMOS technology offers the unity current gain frequency f_T only around 55 GHz. More advanced CMOS technology can be adopted to provide higher speed transistors, but with higher cost. Moreover, the supply voltage shrinks with the technology, making the CMOS design more challenging. Hence, appropriate circuit topologies are required to provide wideband operation using as few passive components as possible, while consuming low power in low voltage.

Many prior studies were proposed for K- and Ka-band applications. Only a few belong to true wideband operation in silicon-based technologies of CMOS and BiCMOS. A 22–29-GHz ultra-wideband (UWB) pulse-radar receiver in 0.18-μm CMOS was proposed using a multistage low-noise amplifier (LNA) with the $C_{\rm gd}$ neutralization technique [1]. However, the proposed circuit requires many inductors, resulting in large area. A receiver front-end using a two-stage LNA and microstrip lines is shown to work from 21 to 29 GHz [5]. Nevertheless, the front-end is bulky because it uses area-consuming transmission lines for impedance matching. A dual-band 24/31-GHz receiver is presented by combining a wideband two-stage LNA and a wideband mixer in a 0.18-μm BiCMOS process [6]–[8]. The reported circuit adopts a single-balanced mixer. Hence, LO leakages might desensitize the following stages. A wideband LNA was reported using resistive feedback to work well in the K-band [9]. It still requires a wideband mixer and a wideband balun to realize a wideband receiver.

The architectures of the aforementioned circuits demand multistage amplifiers to tackle the low f_T issue. Many inductors or transmission lines are necessary to sustain a wideband response. However, utilizing a large number of passive components not only introduces high signal loss, but also occupies large chip area. Power consumption is inevitably increased to compensate the loss for enough gain. Consequently, proper circuit topologies should be developed to give wideband operation while dissipating low power and featuring a small form factor.

Using the technique of resonator coupling is a promising alternative for wideband operation. Recently, the resonator coupling technique is widely exploited to increase the transmission distance in the wireless power transfer application [10]–[13]. It is also applied to circuits for wireless communication systems, such as a narrowband receiver front-end [14], a wideband LNA design [7], an output load of the mixer [15], a low-power narrowband down-conversion mixer [16], a wideband multimode voltage-controlled oscillator (VCO) [17], and a low noise quadrature VCO [18]. Circuit design, however, is usually assumed to be under a symmetric load condition, which is not necessarily true in many realistic circuit implementations. Furthermore, few physical insights on wideband operations are given.

In this paper, a compact 20–30-GHz receiver front-end is designed by using a resonator coupling network (RCN) placed between the LNA and the mixer to realize inter-stage matching. It

Manuscript received April 12, 2012; revised August 19, 2012; accepted August 22, 2012. Date of publication September 17, 2012; date of current version October 29, 2012. This work was supported by the National Science Council, Taiwan, under Grant NSC 100-2220-E-009-013 and Grant NSC 100-2220-E-009-056, by the Ministry of Education in Taiwan under the Aiming for the Top University (ATU) Program, and by MediaTek Inc. under a fellowship.

C.-H. Li and C.-N. Kuo are with the Department of Electronics Engineering and the Institute of Electronics, National Chiao Tung University, Hsinchu 300, Taiwan (e-mail: chli.ee99g@nctu.edu.tw; cnkuo@mail.nctu.edu.tw).

M.-C. Kuo is with the Information and Communications Research Laboratories (ICL), Division for Biomedical and Industrial Integrated Circuit Technology, Industrial Technology Research Institute (ITRI), Hsinchu 310, Taiwan (e-mail: mck@itri.org.tw).

Color versions of one or more of the figures in this paper are available online at http://ieeexplore.ieee.org.

Digital Object Identifier 10.1109/TMTT.2012.2216285

only requires two coupled resonators to support wideband operation. The coupled resonators form a high-order filter to perform functions of a wideband load and wideband impedance transformation simultaneously. Moreover, they act as a wideband balun without paying additional power in realizing single-to-differential conversion. All of the design effort enables the receiver to be realized with a small form factor and low power consumption.

The RCN with an asymmetric load condition is analyzed in detail to provide design guidelines. Analytic formulas for the critical coupling condition, passive gain, peak gain frequency separation (FS), and Ripple are presented. In contrast to the conventional coupled-resonator filter design that is commonly applied for narrowband operation [19], the proposed methodology can be adopted for wideband design with a simple and insightful design process. This paper is organized as follows. Section II details the theory of the inductively coupled resonators (ICRs), including the proposed design flow. In Section III, the consideration of the receiver architecture and the design of each building block are presented. The experimental result is shown in Section IV. Finally, Section V concludes this study.

II. Theory of ICRs

An RCN is employed to transfer a signal, in current, voltage, or power domain, from one resonator to the other, as indicated in Fig. 1(a), in which R_S and R_L represent the source and load resistances, respectively. The coupling is conducted either by an inductor L_C or a capacitor C_C. The ICR is especially attractive since it can be realized by an on-chip transformer. This not only leads to small chip area, but also provides single-to-differential conversion without dissipating any power. The RCN is widely adopted to increase the frequency selectivity in bandpass filter design [19]. It can also provide passive gain by impedance transformation, which is particularly attractive to low-power applications [14].

The typical frequency response of the ICR exhibits resonance frequencies of two oscillatory modes at ω_L and ω_H, as illustrated in Fig. 1(b). If the critical coupling condition is met, the gain levels at ω_L and ω_H are maximum and equal. This implies that the impedance is matched concurrently at ω_L and ω_H for both the input and output ports. The peak-to-peak variation, i.e., Ripple, is defined as

$$\text{Ripple} \equiv G_{\max} - G_{\min} \tag{1}$$

where $G_{\max}$ is the maximum gain and $G_{\min}$ is the minimum gain at the frequency of ω_{min}. If Ripple is less than 3 dB, the ICR response can be considered as wideband.

In this study, the design goal is therefore to make the critical coupling condition occur at two widely separated ω_L and ω_H simultaneously, and keep Ripple within 3 dB. Although only the ICR case is considered as follows, the same approach can also apply to the capacitively coupled resonators.

A. ICR Without Loading Effect

Fig. 2(a) shows the ICR circuit of double resonance. One resonator, L_1 and C_1, is coupled to the other, L_2 and C_2, magnetically. Without loss of generality, the transformer is assumed

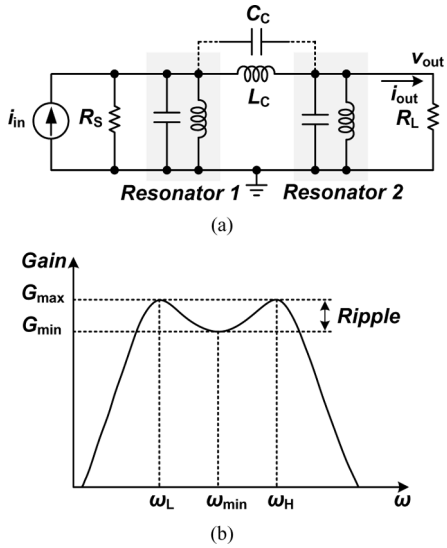

Fig. 1. (a) RCN. The network is coupled either inductively or capacitively. (b) Typical frequency response of the RCN. *Gain* can be current, voltage, or power gain. ω is the radian frequency.

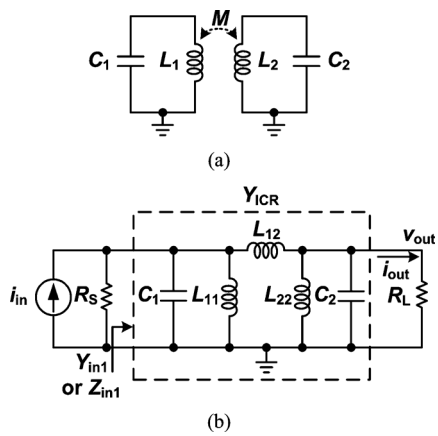

Fig. 2. (a) Network of ICRs. (b) Equivalent circuit of the coupled resonators as the transformer is replaced by its π-model.

lossless. The coupling coefficient k is defined by the mutual inductance M between the two coils as [14]

$$k \equiv \frac{M}{\sqrt{L_1 L_2}}. \tag{2}$$

Let the resonance frequencies of the uncoupled resonators be defined, respectively, as ω_{u1} and ω_{u2} with the frequency ratio of $m \equiv \omega_{u1}/\omega_{u2}$ [14].

Taking the mutual coupling effect into account, the natural resonance frequencies of the coupled network change. They can be derived in terms of m, k, and ω_{u2}, as ω_{uL} and ω_{uH} [14]. The governing equation of the resonance frequencies is established as

$$\left(\frac{\omega_{uL}}{\omega_{u2}}\right)^2 + \left(\frac{\omega_{uH}}{\omega_{u2}}\right)^2 = \frac{1+m^2}{1-k^2}. \tag{3}$$

Consider the coupled resonators in a circuit to analyze signal transfer, as shown in Fig. 2(b). The transformer is replaced with

its π-model equivalent circuit, in which L_{11}, L_{12}, and L_{22} is related to L_1 and L_2 [20].

The critical coupling condition occurs provided that the ICR input is impedance matched to the source, or $Z_{\rm in1} = R_S$, at ω_{uL} and ω_{uH} [14]. It leads to

$$\begin{aligned} Z_{\rm in1}|_{\omega=\omega_{uL,uH}} &= \left\{\frac{n}{k}\left[1-(1-k^2)\left(\frac{\omega_{uL,uH}}{\omega_{u2}}\right)^2\right]\right\}^2 \\ R_L &= R_S \end{aligned} \tag{4}$$

where n is the coil turn ratio of the transformer, defined as

$$n \equiv \sqrt{\frac{L_1}{L_2}}. \tag{5}$$

From (4), another governing equation of ω_{uL} and ω_{uH} is obtained as

$$\left(\frac{\omega_{uL}}{\omega_{u2}}\right)^2 + \left(\frac{\omega_{uH}}{\omega_{u2}}\right)^2 = \frac{2}{1-k^2}. \tag{6}$$

It concludes from (3), (4), and (6) that the critical coupling condition of the ICR can be acquired at both ω_{uL} and ω_{uH} if

$$L_1C_1 = L_2C_2 \tag{7}$$

$$n^2 = \frac{R_S}{R_L}. \tag{8}$$

Namely, those uncoupled resonators need to have the same resonance frequencies, i.e., $m = 1$, and n^2 must be equal to the impedance transformation ratio.

B. ICR With Loading Effect

Resonance occurs at the frequencies that the imaginary part of the input admittance equals to zero. The resistor load in Fig. 2(b) actually affects the resonance frequencies such that ω_{uL} and ω_{uH} need to be modified. The effect becomes severe especially when the loaded quality factor is low for wideband operation. Note that (7) and (8) still hold for achieving critical coupling at resonance frequencies, even with the loading effect.

The two-port admittance matrix of the ICR, $Y_{\rm ICR}$, is used to derive the modified resonance frequencies in Fig. 2(b). The optimal transfer occurs when $Y_{\rm in1} = G_s = 1/R_s$. This input admittance $Y_{\rm in1}$ can be derived from the admittance matrix by

$$Y_{\rm in1} = y_{11} - \frac{y_{21}^2 R_L}{1 + y_{22}R_L}. \tag{9}$$

Given the critical coupling condition by (7) and (8), the matrix elements of $Y_{\rm ICR}$ can be easily shown as

$$\begin{aligned} y_{11} &= \frac{Q}{R_S}\left(\frac{s}{\omega_o} + \frac{\omega_o}{s}\right) \\ y_{22} &= \frac{Q}{R_L}\left(\frac{s}{\omega_o} + \frac{\omega_o}{s}\right) \\ y_{21} &= y_{12} = \frac{-M}{L_1L_2 - M^2}\frac{1}{s} = -\frac{k\omega_o Q}{\sqrt{R_S R_L}}\frac{1}{s} \end{aligned} \tag{10}$$

where Q and ω_o are defined as

$$\begin{aligned} Q &\equiv R_S C_1 \omega_o \\ &= R_L C_2 \omega_o \\ \omega_o &\equiv \frac{1}{\sqrt{L_1C_1(1-k^2)}} \\ &= \frac{1}{\sqrt{L_2C_2(1-k^2)}}. \end{aligned} \tag{11}$$

Essentially Q corresponds to the quality factor of the uncoupled loaded resonators.

Let the imaginary part of the input admittance be zero. The solution gives the modified resonance frequencies of the ICR with the loading effect. Two parallel $\omega_{L,H}$ and one series ω_S[1] resonance frequencies can therefore be found. They are

$$\omega_{L,H} = \omega_o\sqrt{1 - \frac{1}{2Q^2} \pm \sqrt{\left(1-\frac{1}{2Q^2}\right)^2 - (1-k^2)}} \tag{12}$$

$$\omega_S = \omega_o. \tag{13}$$

When Q is high, (12) can be simplified as

$$\omega_{L,H} = \omega_o\sqrt{(1 \pm k)}. \tag{14}$$

As expected, (14) is the same as ω_{uL} and ω_{uH} when $m = 1$, indicating that the loading effect can be neglected.

At ω_L and ω_H, the input admittance $Y_{\rm in1}$ becomes a real value, given by

$$Y_{\rm in1}|_{\omega_L,\omega_H} = G_S = \frac{1}{R_S}. \tag{15}$$

The impedance matching condition is achieved. The ICR can couple the signal with the highest gain. This confirms the critical coupling condition in (7) and (8), even with the loading effect. In essence, this is an impedance transformation process to meet the optimal loading condition. On the other hand, impedance transformation is different at ω_S. The input impedance is given as

$$Y_{\rm in1}|_{\omega_S} = G_S\,(kQ)^2 \tag{16}$$

which fails to meet the critical coupling condition. That is, energy coupling is less efficient than that at ω_L and ω_H.

Note that $\omega_{L,H}$ coincides with ω_S at ω_o as $kQ = 1$. Although it appears that the critical coupling condition is achieved at ω_S as $kQ = 1$, the coupling system exhibits a narrowband response, undesired for the wideband operation. It is also observed that ω_S is very close to the minimum gain frequency $\omega_{\rm min}$ as Q is high and k is small.

C. Signal Gain

The passive coupled system in Fig. 2(b) can give signal current or voltage gain, utilizing impedance transformation. This passive gain by the impedance transformation is very useful for the low power application since it does not consume any power.

[1]Strictly speaking, ω_S is not considered as a resonance frequency of the coupling system since the highest gain is not gained at it in most case, except as $kQ = 1$ as indicated in (16).

Consider all of the available power from the source is delivered to the load, i.e.,

$$\frac{1}{2}(i_{\text{out}})^2 R_L = \frac{1}{2}\left(\frac{1}{2}i_{\text{in}}\right)^2 R_S. \tag{17}$$

If $R_L < R_S$, it yields to the maximum current gain given by

$$A_{I,\max} = \frac{i_{\text{out}}}{i_{\text{in}}} = \frac{1}{2}\sqrt{\frac{R_S}{R_L}}. \tag{18}$$

If $R_L > R_S$, it achieves the maximum voltage gain given by

$$A_{V,\max} = \frac{v_{\text{out}}}{v_{\text{in}}} = \frac{1}{2}\sqrt{\frac{R_L}{R_S}}. \tag{19}$$

The maximum gain is obtained under the impedance matching condition.

An ideal transformer gives the maximum gain in the broadband sense. If the turn ratio is set as $\sqrt{R_S/R_L}$ for the impedance transformation, the maximum current gain can be obtained over infinite bandwidth. In the case of an RCN, the maximum gain occurs only at the resonance frequencies calculated by (12). Gain decreases to a minimum between the two peak gain frequencies, resulting in gain variation. It is critical to make wide separation between the peak gain frequencies, and keep Ripple less than 3 dB.

The closed form of the ICR current gain can be derived as

$$\frac{i_{\text{out}}}{i_{\text{in}}} = \frac{-y_{21}}{(G_S + y_{11})(1 + y_{22}R_L) - y_{21}^2 R_L}. \tag{20}$$

After substituting (10) into (20), the current gain can be shown as

$$\frac{i_{\text{out}}}{i_{\text{in}}} = \frac{-j2kQ\omega_n}{\left\{\omega_n\left[1 + jQ\left(\omega_n - \frac{1}{\omega_n}\right)\right]\right\}^2 + (kQ)^2}\frac{1}{2}\sqrt{\frac{R_S}{R_L}} \tag{21}$$

where ω_n is the frequency normalized to ω_o, i.e., $\omega_n \equiv \omega/\omega_o$. The voltage gain can also be derived by transforming the Norton current source into the Thevenin voltage. Note that the derived gain formulas are exactly matched to the simulation results. It is quite cumbersome to formulate the closed form of the minimum passive gain. Instead, the results are observed numerically. The normalized current gain using (18) and (21) is plotted in Fig. 3, where k and Q are varied.

It is clear that the minimum gain occurs at the frequency of $\omega_{\min} \neq 1$, i.e., not equal to ω_o. By observing the gain response, $\omega_{\min}$ is approximately at $(\omega_L + \omega_H)/2$, the arithmetic average of ω_L and ω_H. From (18) and (21), Ripple can be acquired as

$$\text{Ripple} = 20\log\left|\frac{\left\{\omega_m\left[1 + jQ\left(\omega_m - \frac{1}{\omega_m}\right)\right]\right\}^2 + (kQ)^2}{-j2kQ\omega_m}\right| \tag{22}$$

where $\omega_m = \omega_{\min}/\omega_o$. For convenience, we define a parameter of FS as

$$\text{FS} \equiv \frac{\omega_H - \omega_L}{\omega_{\min}} \times 100\% = 2\left(\frac{\omega_H - \omega_L}{\omega_H + \omega_L}\right) \times 100\%. \tag{23}$$

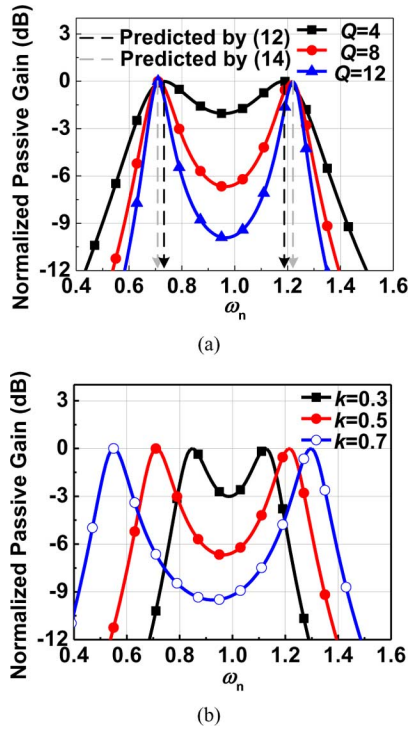

Fig. 3. Normalized passive gain versus ω_n. (a) k is fixed at 0.5. (b) Q is fixed at 8.

Note that the actual -3-dB bandwidth is wider than (23) since ω_L and ω_H correspond to the highest gain that the RCN can provide. It is evident that the resonance frequencies are affected by Q, the loading effect, and k, the coupling. Higher FS can be obtained if the coupling is stronger, but larger Ripple is also introduced. On the other hand, smaller k and Q result in smaller Ripple at the price of narrower FS. Obviously, there exists a tradeoff between FS and Ripple to meet a desired wideband response with an acceptable Ripple level. Fig. 4 shows the comparison between simulation and calculation results of FS and Ripple as k and Q are varied. The calculation results match well with simulation ones.

Contour plots can help designers to choose an appropriate combination of k and Q to trade off FS and Ripple. Two plots in Fig. 5 are superposed over the range of Q and k from 0 to 15 and 0 to 1, respectively. The *No Solution* region represents that the ICR no longer resonates at ω_L and ω_H, but only at ω_o. Actually, it is bounded by $kQ = 1$, corresponding to zero FS. The contour line of 3-dB Ripple is highlighted via a blue line (in the online version) with circular symbols. The associated component values are summarized in Table I. These parameters are normalized to R_S and ω_o so that they can be easily scaled to the frequency band of interest.

D. Design Flow of the ICR

With the derived transfer functions, FS, and Ripple, the ICR for the wideband impedance transformation can be designed systematically. In the first place, the coil turn ratio n is selected according to the R_S/R_L ratio. Given the targeted FS and the acceptable Ripple, the values of Q and k can be determined. $\omega_{\min}$ is obtained since it locates at the center of the interested

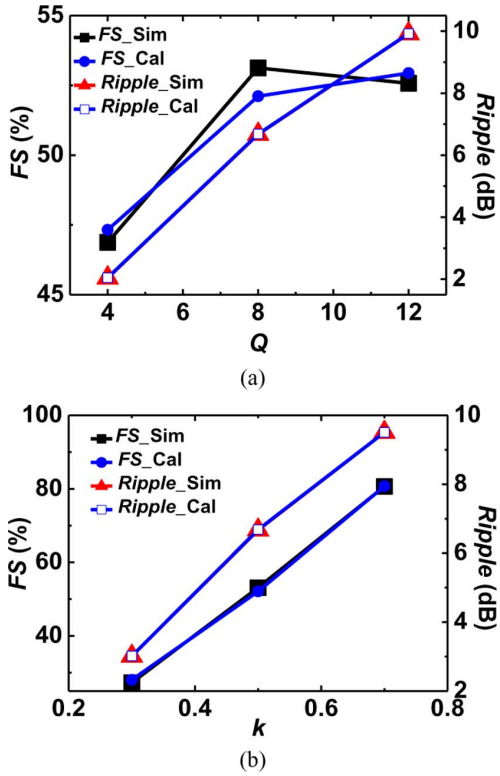

Fig. 4. Comparison between simulation and calculation results of FS and Ripple. (a) k is fixed at 0.5. (b) Q is fixed at 8.

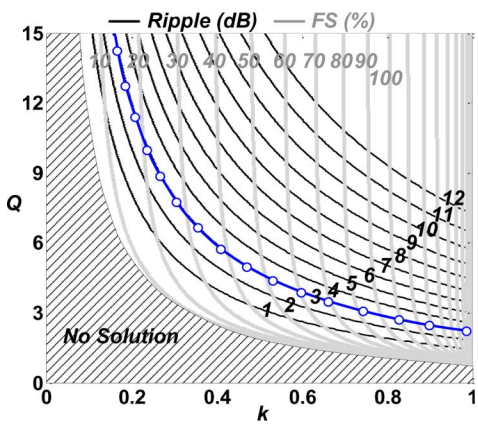

Fig. 5. Contour plots of FS and Ripple versus the coupling coefficient and the quality factor of Q.

band. ω_o is then found from $\omega_{\min}$. From (11), C_1, C_2, L_1, and L_2 can be determined exactly. A transformer is designed to meet the component values. Additional capacitors can be added if the extracted parasitic capacitance does not meet the requirement. The design flow of the ICR is summarized in Fig. 6.

The properties of compact chip area, wideband impedance transformation, and working as a balun make the ICR very suitable for on-chip circuit design. Hence, the ICR is incorporated into the proposed wideband receiver front-end to realize a compact, low power, and low-cost solution. Section III is going to present the details of the receiver design.

TABLE I
COMPONENT VALUES FOR 3-dB RIPPLE

$R_S/R_L = n^2$, $C_{n2} = n^2 C_{n1}$, $L_{n2} = L_{n1}/n^2$, $C_1 = C_{n1}/R_S\omega_o$, $C_2 = C_{n2}/R_S\omega_o$, $L_1 = R_S L_{n1}/\omega_o$, and $L_2 = R_S L_{n2}/\omega_o$.				
k	Q	FS (%)	L_{n1}	C_{n1}
0.1	24.09	9.1	0.04	24.09
0.2	12.02	18.4	0.09	12.02
0.3	7.98	28.0	0.14	7.98
0.4	5.96	38.2	0.20	5.96
0.5	4.73	49.2	0.28	4.73
0.6	3.90	61.5	0.40	3.90
0.7	3.30	75.9	0.59	3.30
0.8	2.85	93.8	0.97	2.85
0.9	2.48	119.4	2.12	2.48

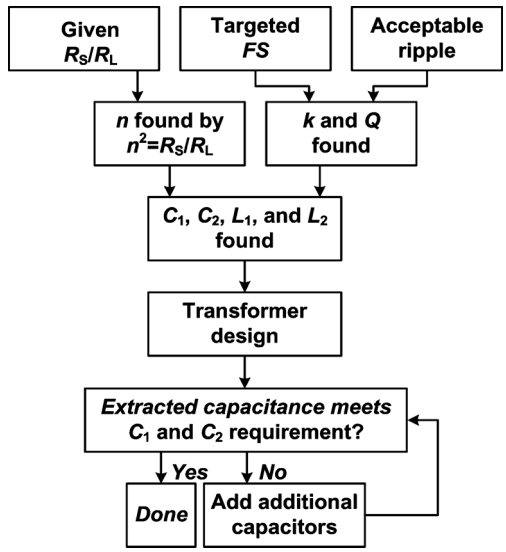

Fig. 6. Design flow of the ICR for wideband applications.

III. WIDEBAND RECEIVER DESIGN

The receiver architecture under consideration is shown in Fig. 7 [14]. The direct-conversion architecture is adopted for the sake of a minimal number of components. It also eliminates the need of an image rejection filter. In this study, only the I-path is implemented, including an LNA, a balun, and a double-balanced mixer. The Q-path can be easily incorporated by using the same design. The design needs to provide wideband responses of voltage-to-current conversion in the LNA stage, single-to-differential conversion in the balun, and current-to-voltage frequency conversion in the mixer. Hence, poles associated with the LNA output capacitance $C_{\rm LNA}$, the mixer input capacitance $C_{\rm Mixer}$, and other parasitic ones, shall be considered carefully.

Fig. 8 shows the proposed wideband receiver front-end. Low power operation is feasible since it only needs a few passive components and amplifier stages. The LNA adopts a common-gate (CG) topology, which gives a wideband response not only in gain, but also in noise and linearity. It also directly works as the transconductor stage of the mixer, which is a great benefit in reducing power consumption [14]. The ICR fulfills the balun function and inter-stage impedance transformation. Actually the two coupled resonators absorb the parasitic capacitances from the LNA, transformer, and mixer into the design, which is favorable for bandwidth enhancement of alleviating the issue

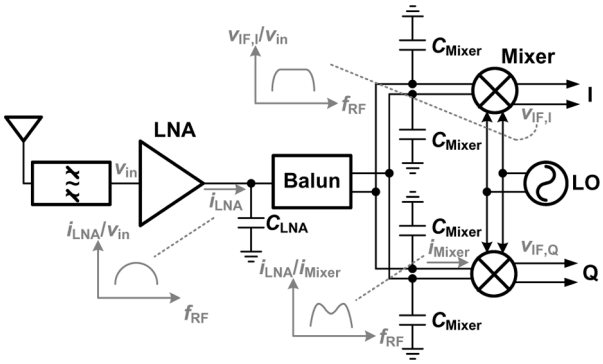

Fig. 7. Adopted direct-conversion architecture. This study includes the design of an LNA, a balun, and a mixer in the I-path.

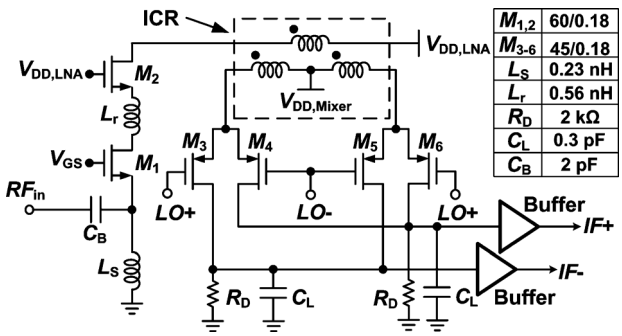

Fig. 8. Proposed wideband receiver front-end. The ICR functions as a balun and also provides wideband impedance transformation. C_B is used as a dc blocking capacitor.

due to the mixer input pole and the LNA output pole. Finally, the double-balanced mixer provides the frequency down-conversion and eliminates LO leakages from desensitizing the following stages [14]. The Sections III-A–III-C will detail each block design.

A. LNA Design

The LNA is a critical block to provide a wideband response, not only in input matching but also in noise figure (NF) and linearity. It was proposed to apply a common-source (CS) structure with a high-order input matching network for wideband operation [21], [22]. However, the approach calls for a large number of inductors, requiring large chip area and increasing NF. In this study, the common-gate low-noise amplifier (CG-LNA) is instead chosen, which is in need of only one inductor. The CG-LNA is also advantageous because it has better reverse isolation and stability [23]. The most significant feature is that it provides better noise performance for higher operating frequency $\omega_{\rm op}$ since the gate-induced noise is insensitive to $\omega_{\rm op}/\omega_T$ (ω_T is the unity current gain frequency) while the CS-LNA is proportional to $\omega_{\rm op}/\omega_T$ [24].

The input equivalent circuit of the CG-LNA is established to analyze the input matching, as shown Fig. 9(a), in which R_S is the source resistance and $C_{\rm gs1}$ and g_{m1} are the gate-to-source capacitance and the transconductance of M_1, respectively. It requires g_{m1} equal to $1/R_S$ for impedance matching. L_S tunes out $C_{\rm gs1}$ only at the center of the frequency band. Wideband

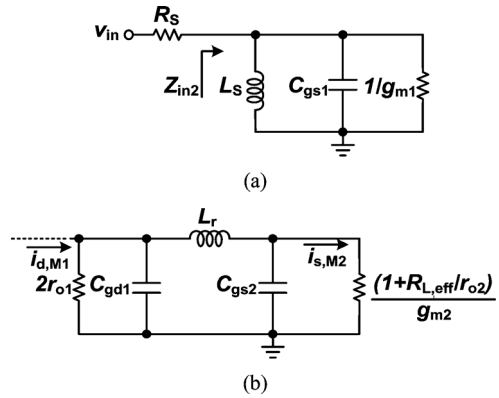

Fig. 9. (a) Equivalent circuit for the input matching network. (b) Equivalent circuit for the matching network at the M_1 drain.

matching relies on the low quality factor of the input matching network. The input impedance $Z_{\rm in2}(s)$ can be derived as

$$Z_{\rm in2}(s) = \frac{\dfrac{s}{C_{\rm gs1}}}{s^2 + \left(\dfrac{\omega_{oi}}{Q_{\rm in}}\right) s + \omega_{oi}^2} \tag{24}$$

where $Q_{\rm in}$ and ω_{oi} are defined as

$$\begin{aligned} Q_{\rm in} &\equiv \frac{\omega_{oi} C_{\rm gs1}}{g_{m1}} = \omega_{oi} C_{\rm gs1} R_S \\ \omega_{oi} &\equiv \frac{1}{\sqrt{L_S C_{\rm gs1}}} \end{aligned} \tag{25}$$

representing the quality factor and the resonance frequency of the input matching network, respectively. To have bandwidth of $0.4\omega_{oi}$, i.e., 40%, $Q_{\rm in}$ needs to be smaller than 2.5. Note that the above derivation assumes infinite output resistance r_o. If r_o is finite, the loading at the M_1 drain will affect the input matching. L_S can be adjusted to move ω_{oi} back to the desired frequency.

The parasitic capacitance at the drain node of M_1 introduces a nondominant pole and degrades the LNA bandwidth. For bandwidth enhancement, the inductor L_r is added to form a π-network together with the gate-to-drain capacitance $C_{\rm gd1}$ of M_1 and the gate-to-source capacitance $C_{\rm gs2}$ of M_2, as shown in Fig. 9(b). The network is driven by the M_1 output short current $i_{d,M1}$ with the impedance of twice of the M_1 output resistance r_{o1}, and loaded by the M_2 input resistance expressed as $1/g_{m2} + R_{L,\rm eff}/(g_{m2} r_{o2})$, where $R_{L,\rm eff}$ is the effective load seen by M_2. The network generates the output current $i_{s,M2}$, equal to the LNA output current $i_{\rm LNA}$ through the CG M_2 transistor. Smaller L_r values present wider bandwidth of the current transfer, but with the price of larger gain ripple [25]. In this study, the network is intentionally designed to provide gain peaking around 28 GHz for the concern of higher ICR loss at ω_H in practice.

Adding L_r can also minimize the variation of the LNA noise within the interested band. The NF is dominated by M_1 in the low operating frequency. M_2 noise can be neglected because of high degeneration impedance at its source. However, the degeneration impedance decreases at the high operating frequency due to the parasitic pole at the M_1 drain. This causes M_2 noise contribution to rise rapidly along with the frequency. L_r boosts

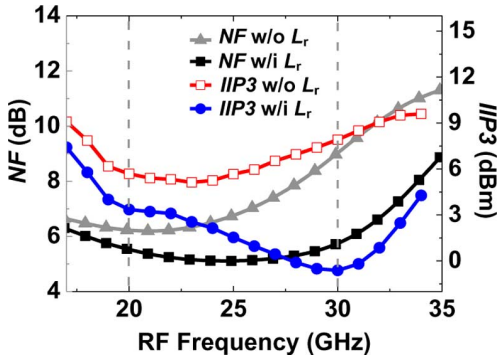

Fig. 10. Frequency response of the NF and IIP3 as L_r either is or is included.

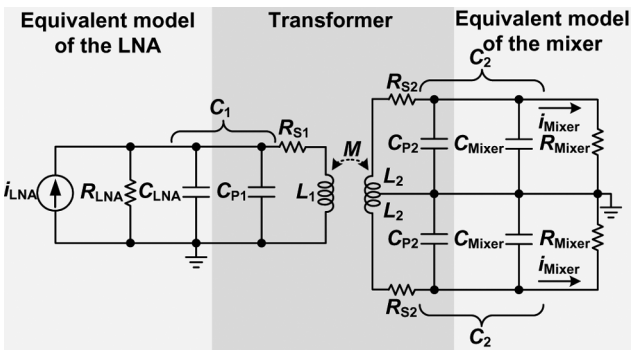

Fig. 11. Equivalent circuit of the ICR.

the LNA gain at ω_H and also helps suppress M_2 noise. Hence, the noise can be assumed to be mainly contributed by the M_1 transistor. Accordingly, the noise factor can be derived as

$$F = 1 + \frac{\gamma}{\alpha} + \frac{\delta\alpha}{5}\left(\frac{\omega_o}{\omega_T}\right)^2 \tag{26}$$

where r, α, and δ are process-dependent noise parameters [26]. F is dominated by the second factor associated with the channel thermal noise. The only frequency-dependent term is the third one, which has a small weighting factor, implying less sensitivity of the NF to the frequency variation. Actually, noise matching only occurs within a narrow frequency range since no feedback technique is employed. However, L_r can minimize the NF variation within the interested frequency band. Fig. 10 shows the post-layout simulation results of the NF frequency response with and without L_r. The variation becomes smaller than 0.63 dB over the 20–30-GHz band after L_r is added.

For the linearity consideration, the CG-LNA has a superior input third-order intercept point (IIP3) as compared to the CS counterpart [27]. In general, the linearity is strongly affected by the LNA output loading [14]. That is, the IIP3 is insensitive to the frequency variation as long as the LNA faces a wideband load. In this study, the wideband load is achieved by the ICR to sustain wideband linearity performance. Fig. 10 shows the post-layout simulation results of the IIP3 with and without L_r as the LNA is loaded with the ICR and the mixer. The IIP3 is degraded as L_r is included. However, the IIP3 is still better than -0.6 dBm. It is worth trading off the linearity for the NF improvement.

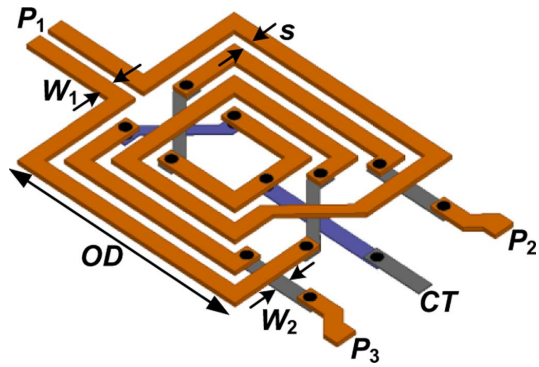

Fig. 12. Proposed transformer. W_1, W_2, and s are the width and spacing of the primary and secondary coils, respectively. *OD* is the outside dimension.

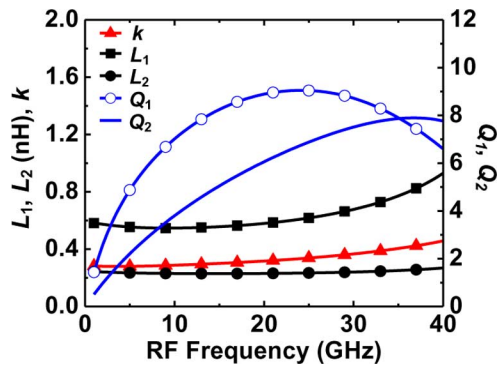

Fig. 13. EM simulation results of the proposed transformer.

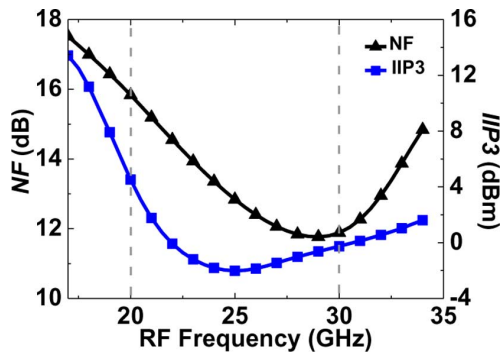

Fig. 14. Post-layout simulation results of the NF and the IIP3 of the mixer.

Based on the above discussion, the bias and the transistor size can be designed accordingly. To make g_{m1} equal to $1/R_S$, the transistor with higher $V_{\rm GS}$ and smaller size can be chosen or vice versa. A smaller transistor can increase the matching bandwidth, but at the price of higher power consumption and larger L_S. On the other hand, the power consumption can be reduced by choosing a larger transistor, but at the cost of narrower bandwidth and higher noise. To make good tradeoff among the power, NF, and chip area, the bias and the transistor size are designed as 0.77 V and 60 μm, respectively. L_S of 0.23 nH is employed to resonate at around 25 GHz. The quality factor is calculated to be 1.4, corresponding to the bandwidth of 17.8 GHz. The LNA only draws 3.8 mA from a 1.2-V supply.

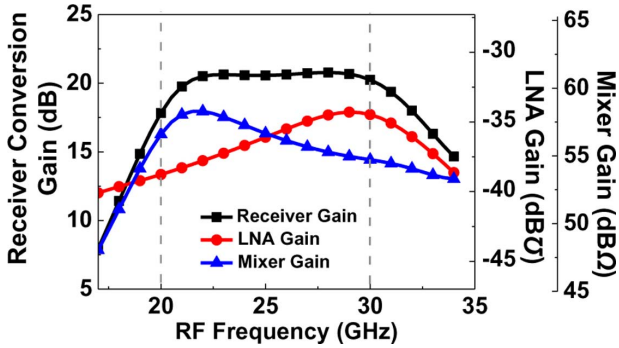

Fig. 15. Gain response of each building block, including the LNA, the mixer (including the ICR), and the whole receiver front-end.

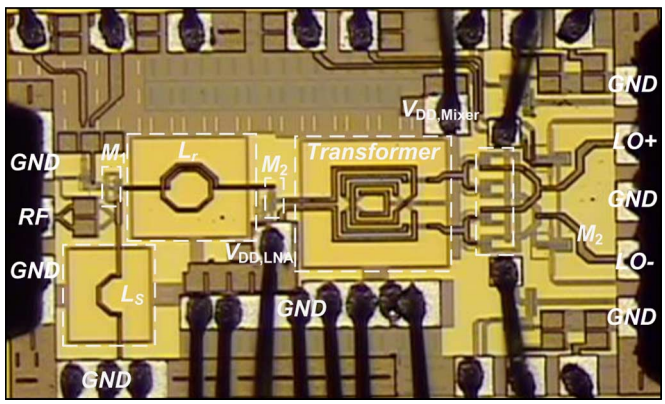

Fig. 16. Chip micrograph of the proposed receiver front-end.

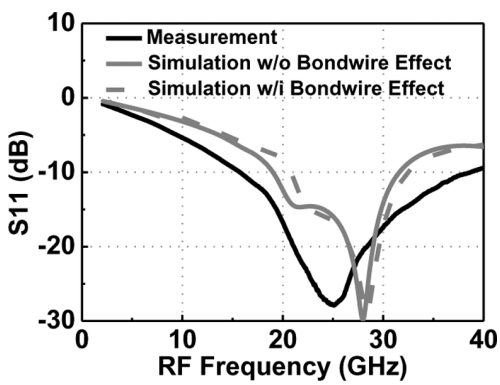

Fig. 17. Measured input return loss.

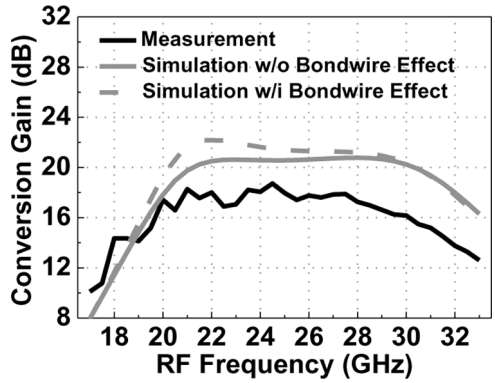

Fig. 18. Measured RF bandwidth.

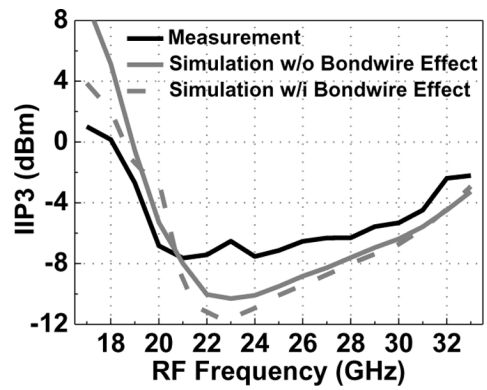

Fig. 19. Measured IIP3.

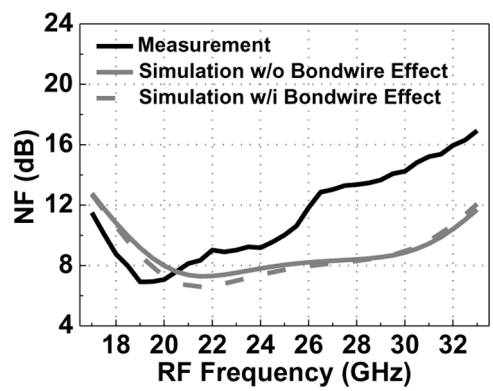

Fig. 20. Measured NF.

B. Mixer Design

The mixer is implemented in the doubled-balanced configuration for better port-to-port isolation. This is especially critical for the direct conversion receiver. In this study, the LNA is directly utilized as the transconductor stage to reduce the power consumption. Since the mixer linearity is mainly bounded by the transconductor stage, the CG-LNA also benefits in mixer performance due to the degeneration resistance R_S.

$M_{3–6}$ transistors act as the switching stage. pMOS transistors are chosen because of better flicker noise performance. Ideally, only one switching path is on at a time. Nonideal switching, however, degrades the noise and the gain performance. To reduce the time interval in which the switching transistors are on simultaneously, local oscillator (LO) power of -1 dBm and $V_{SG,3–6}$ of 0.49 V, near the transistor threshold voltage, are chosen. R_D and C_L are designed as 2 kΩ and 0.3 pF, resulting in IF bandwidth around 300 MHz.

C. ICR Design

Once the design of the mixer and the LNA is completed, the ICR is employed to provide wideband signal transfer. Fig. 11 illustrates the equivalent-circuit model [14]. The output and the input impedances of the LNA and the mixer are modeled by R_{LNA}, C_{LNA}, R_{Mixer}, and C_{Mixer}, respectively. C_{P1}, C_{P2}, R_{S1}, and R_{S2} model the parasitic capacitances and the ohmic losses of the transformer, respectively. To ease the analysis, the transformer is assumed lossless. Since the transformer is symmetric to the virtual ground of the secondary coil, the ICR can

TABLE II
PERFORMANCE SUMMARY AND COMPARISON WITH PRIOR STUDIES

Reference	Technology (f_T (GHz))	V_{DD} (V)	P_{DC} (mW)	RF Frequency (GHz)	-3-dB BW *(%)*	*S*11 (dB)	Gain (dB)	IIP3 (dBm)	NF (dB)	Active Area (mm^2)
[1]	0.18 μm CMOS (55)	1.8	32.9[a]	21.3-29	30.6	< -14.5	28.1	> -9	5.5-7.4	2.5[b]
[2]	0.18 μm CMOS (55)	1.5	60	21.8	--	-21.8	35.7	-13.5[c]	7.7	0.2
[5]	0.18 μm CMOS (55)	1.8	39.2	21-29	32	< -8.8	25.1	-17.9	4.1-5.1	0.96
[6]	0.18 μm BiCMOS (70)	1.8	60	24/31	--	< -12	21/18	N/A	8/9.5	0.7
[29][d]	SiGe HBT (80)	5.0	1080	22-26	16.7	< -5	45	N/A	7.8	N/A
[30]	0.13 μm CMOS (NA)	1.5	115	22-24	8.7	< -10	12	> -12.5	7.5-8	0.75[e]
[31]	65 nm CMOS (NA)	N/A	69.6	23-25	8.3	N/A	31.5	-17	6.5	0.35[e]
[32]	0.13 μm CMOS (NA)	1.6	45.8	24	--	-15	3.2	-3.2[c]	10	0.29
[33]	0.18 μm CMOS (55)	1.8	54	24	--	-14.3	28.4	-13	6	0.81
[34]	0.18 μm BiCMOS (200)	2.5	107.5	22-29	27.5	< -10	35	-23.7[c]	4.5-5.7	N/A
This Work	**0.18 μm CMOS (55)**	**1.2**	**5.2**	**20-30**	**40**	**< -17.6**	**18.7**	**> -7.6**	**7.1-14.2**	**0.18**

(a) including the variable-gain amplifier (VGA) power. (b) including I/Q paths. (c) estimated by IIP3~ P1dB + 9.5 dBm. (d) LNA + mixer + VGA + switch + integrator. (e) estimated.

be analyzed by using the upper half circuit of Fig. 11. As compared to Fig. 2, the developed ICR theory can be applied directly here. Following the design flow in Fig. 6, the ICR can be designed systematically. In the first place, the coil turn ratio n is selected as 1.5 due to the $R_{\rm LNA}/R_{\rm Mixer}$ ratio. The targeted FS and the Ripple are around 30% and 3 dB, respectively. From Table I, Q of around 8 and k of 0.3 are chosen. $\omega_{\rm min}$ is located at 25 GHz, the center of the interested band. ω_o is then found to be 25.34 GHz. C_1 of 72 fF, C_2 of 163 fF, L_1 of 0.6 nH, and L_2 of 0.27 nH, are determined accordingly.

The designed transformer is shown in Fig. 12, where the P_1 port is connected to the LNA, and the P_2 and P_3 ports are connected to the double-balanced mixer. The width of the primary and secondary coils, W_1 and W_2, is chosen as 8 μm. The spacing is designed as 6 μm to let k near the desired value of 0.3. The outside dimension *OD* is chosen as 130 μm to fulfill the L_1 and L_2 requirement. The electromagnetic (EM) simulation results of the proposed transformer are illustrated in Fig. 13. The extracted transformer parameters are L_1, L_2, n, k, R_{S1}, and R_{S2} of 0.59 nH, 0.24 nH and 1.6, 0.28, 2.48, and 3 Ω, respectively. Note that L_1, L_2, and k are extracted at low-frequency range as the capacitive effect can be neglected. Since the parasitic capacitances from the LNA, mixer, and transformer are close to the C_1 and C_2 requirement, no additional capacitors are required.

The post-layout simulation results of the NF and the IIP3 of the mixer combined with the ICR are shown in Fig. 14. The NF and IIP3 are varied from 11.8 to 15.8 dB and -2 to 4.5 dBm, respectively, within 20–30-GHz range.

Fig. 15 illustrates the post-layout simulation results of the gain response of each building block, including the trans-conductance gain of the LNA, the trans-resistance gain of the mixer combined with the ICR, and the conversion gain of the receiver front-end. The unavoidable ohmic loss in the ICR causes around 3-dB lower gain at ω_H than that at ω_L. Fortunately, using L_r for bandwidth enhancement in the LNA stage can compensate this effect. The proposed receiver shows -3-dB bandwidth from 20 to 33 GHz with a peak conversion gain of 20.8 dB.

IV. EXPERIMENTAL RESULTS

The wideband receiver front-end is implemented in 0.18-μm CMOS technology with f_T around 55 GHz. The chip micrograph is shown in Fig. 16. The die size is 1000 μm $\times$ 670 μm, including the bonding pads. The active area is only 0.18 mm^2. The measurement is conducted by a chip-on-board setup. DC bias is wire-bonded to a printed circuit board (PCB), while the RF and LO signals are applied using high-frequency probes. The differential IF signal is converted into a single-ended output by an off-chip balun. The front-end only consumes 5.2 mW under a 1.2-V supply.

Fig. 17 shows the measured input return loss. The input return loss is better than 17.6 dB within the 20–30-GHz band. Fig. 18 illustrates the measured conversion gain as the LO power and IF frequency are -1 dBm and 3 MHz, respectively. The peak gain is 18.7 dB with -3-dB bandwidth covering from 20 to 30 GHz. The measured result shows a similar trend as that of the simulated one. The parasitic effect caused by bond-wires between the chip ground and PCB ground is also observed. It results in an uneven frequency response. There exits roughly 3-dB gain difference between the measured and the simulated results. The discrepancy might come from the nonaccurate transistor modeling that causes additional unexpected parasitic components. This might be improved by extracting the transistor parasitic capacitances by using EM simulation [28].

The IIP3 is measured by conducting a two-tone test with an FS of 0.1 MHz. Fig. 19 shows the measured IIP3. It is better than -7.6 dBm within the 20–30-GHz band. 1-dB compression point is also measured. It varied from -15.1 to -17.9 dBm, within the 20–30-GHz frequency range. Fig. 20 illustrates the measured NF as the IF frequency is 10 MHz. The minimum NF is 7.1 dB. The rise of the NF at higher frequency band is caused by the gain degradation. Table II summaries the chip performance and makes a comparison with prior studies. It is clear that the proposed receiver front-end shows the lowest power consumption, lowest supply voltage, and occupies the smallest chip area, while keeping good circuit performance in the gain, input return loss, linearity, and bandwidth.

V. CONCLUSION

A compact low-power wideband receiver front-end using ICRs has been proposed and verified by experimental results. The wideband theory of the ICR with asymmetric loads has been given and guidelines have been provided to design the ICR systematically. Realized in 0.18-μm CMOS technology, the receiver achieves -3-dB bandwidth of 20–30 GHz with a peak gain of 18.7 dB. The power consumption is only 5.2 mW from a 1.2-V supply. The occupied chip area is only 0.18 mm^2.

The proposed technique can be easily applied to other bands, such as the 57–64-GHz band.

ACKNOWLEDGMENT

The authors would like to acknowledge the Chip Implementation Center (CIC), Hsinchu, Taiwan, for chip fabrication and measurement support and ANSYS, Taipei, Taiwan, for design support.

REFERENCES

[1] V. Jain, S. Sundararaman, and P. Heydari, "A 22–29-GHz UWB pulse-radar receiver front-end in 0.18-μm CMOS," *IEEE Trans. Microw. Theory Techn.*, vol. 57, no. 8, pp. 1903–1914, Aug. 2009.

[2] X. Guan and A. Hajimiri, "A 24-GHz CMOS front-end," *IEEE J. Solid-State Circuits*, vol. 39, no. 2, pp. 368–373, Feb. 2004.

[3] A. Nordbotten, "LMDS systems and their application," *IEEE Commun. Mag.*, vol. 38, no. 6, pp. 150–154, Jun. 2000.

[4] H.-Y. Lin, S. S. H. Hsu, C.-Y. Chan, J.-D. Jin, and Y.-S. Lin, "A wide locking-range frequency divider for LMDS applications," *IEEE Trans. Circuits Syst. II, Exp. Briefs*, vol. 54, no. 9, pp. 750–754, Sep. 2007.

[5] S.-L. Huang, Y.-S. Lin, and J.-H. Lee, "A low-power low-noise 21–29 GHz ultra-wideband receiver front-end in 0.18 μm CMOS technology," in *Proc. IEEE Custom Integr. Circuits Conf.*, 2011, pp. 1–4.

[6] M. El-Nozahi, A. Amer, E. Sanchez-Sinencio, and K. Entesari, "A millimeter-wave (24/31 GHz) dual-band switchable harmonic receiver in 0.18-μm SiGe process," *IEEE Trans. Microw. Theory Techn.*, vol. 58, no. 11, pp. 2717–2730, Nov. 2010.

[7] M. El-Nozahi, E. Sanchez-Sinencio, and K. Entesari, "A millimeter-wave (23–32 GHz) wideband BiCMOS low-noise amplifier," *IEEE J. Solid-State Circuits*, vol. 45, no. 2, pp. 289–299, Feb. 2010.

[8] M. El-Nozahi, E. Sanchez-Sinencio, and K. Entesari, "A 20–32-GHz wideband mixer with 12-GHz IF bandwidth in 0.18-μm SiGe process," *IEEE Trans. Microw. Theory Techn.*, vol. 58, no. 11, pp. 2731–2740, Nov. 2010.

[9] H.-K. Chen, Y.-S. Lin, and S.-S. Lu, "Analysis and design of a 1.6–28-GHz compact wideband LNA in 90-nm CMOS using a π-match input network," *IEEE Trans. Microw. Theory Techn.*, vol. 58, no. 8, pp. 2092–2104, Aug. 2010.

[10] A. Kurs *et al.*, "Wireless power transfer via strongly coupled magnetic resonances," *Science*, vol. 317, no. 5834, pp. 83–86, Jul. 2007.

[11] S. Han and D. D. Wentzloff, "Wireless power transfer using resonant inductive coupling for 3-D integrated ICs," in *IEEE Int. Conf. 3-D Syst. Integration*, 2010, pp. 1–5.

[12] A. P. Sample, D. A. Meyer, and J. R. Smith, "Analysis, experimental results, and range adaptation of magnetically coupled resonators for wireless power transfer," *IEEE Trans. Ind. Electron.*, vol. 58, no. 2, pp. 544–554, Feb. 2011.

[13] N. Shinohara, "Power without wires," *IEEE Microw. Mag.*, vol. 12, no. 7, pp. S64–S73, Dec. 2011.

[14] C.-H. Li, Y.-L. Liu, and C.-N. Kuo, "A 0.6-V 0.33-mW 5.5-GHz receiver front-end using resonator coupling technique," *IEEE Trans. Microw. Theory Techn.*, vol. 59, no. 6, pp. 1629–1638, Jun. 2011.

[15] F. Vecchi *et al.*, "A wideband receiver for multi-Gbit/s communications in 65 nm CMOS," *IEEE J. Solid-State Circuits*, vol. 46, no. 3, pp. 551–561, Mar. 2011.

[16] C. Hermann, M. Tiebout, and H. Klar, "A 0.6-V 1.6-mW transformer-based 2.5-GHz downconversion mixer with $+5.4$-dB gain and -2.8-dBm IIP3 in 0.13-μm CMOS," *IEEE Trans. Microw. Theory Techn.*, vol. 53, no. 2, pp. 488–495, Feb. 2005.

[17] B. Catli and M. M. Hella, "A 1.94 to 2.55 GHz, 3.6 to 4.77 GHz tunable CMOS VCO based on double-tuned, double-driven coupled resonators," *IEEE J. Solid-State Circuits*, vol. 44, no. 9, pp. 2463–2477, Sep. 2009.

[18] U. Decanis, A. Ghilioni, E. Monaco, A. Mazzanti, and F. Svelto, "A low-noise quadrature VCO based on magnetically coupled resonators and a wideband frequency divider at millimeter waves," *IEEE J. Solid-State Circuits*, vol. 46, no. 12, pp. 2943–2955, Dec. 2011.

[19] J.-S. Hong and M. J. Lancaster, *Microstrip Filters for RF/Microwave Applications*. New York: Wiley, 2001.

[20] C. Alexander and M. Sadiku, *Fundamentals of Electric Circuits*, 2nd ed. New York: McGraw-Hill, 2004.

[21] A. Bevilacqua and A. M. Niknejad, "An ultrawideband CMOS low noise amplifier for 3.1–10.6 GHz wireless receiver," *IEEE J. Solid-State Circuits*, vol. 39, no. 12, pp. 2259–2268, Dec. 2004.

[22] A. Ismail and A. A. Abidi, "A 3–10 GHz low noise amplifier with wideband *LC*-ladder matching network," *IEEE J. Solid-State Circuits*, vol. 39, no. 12, pp. 2269–2277, Dec. 2004.

[23] D. J. Allstot, X. Li, and S. Shekhar, "Design consideration for CMOS low noise amplifiers," in *Proc. IEEE RFIC Symp.*, 2004, pp. 97–100.

[24] W. Zhuo *et al.*, "A capacitor cross-coupled common-gate low noise amplifier," *IEEE Trans. Circuits Syst. II, Exp. Briefs*, vol. 52, no. 12, pp. 875–879, Dec. 2005.

[25] B. Analui and A. Hajimiri, "Bandwidth enhancement for transimpedance amplifiers," *IEEE J. Solid-State Circuits*, vol. 39, no. 8, pp. 1263–1270, Aug. 2004.

[26] T. H. Lee, *The Design of CMOS Radio-Frequency Integrated Circuits*, 2nd ed. New York: Cambridge Univ. Press, 2004.

[27] H. Zhang, X. Fan, and E. S. Sinencio, "A low-power, linearized, ultra-wideband LNA design technique," *IEEE J. Solid-State Circuits*, vol. 44, no. 2, pp. 320–330, Feb. 2009.

[28] C. Liang and B. Razavi, "Systematic transistor and inductor modeling for millimeter-wave design," *IEEE J. Solid-State Circuits*, vol. 44, no. 2, pp. 450–457, Feb. 2009.

[29] I. Gresham, N. Kinayman, A. Jenkins, and R. Point, "A fully integrated 24 GHz SiGe receiver chip in low-cost QFN plastic package," in *Proc. IEEE RFIC Symp.*, 2006, pp. 329–332.

[30] T. Yu and G. M. Rebeiz, "A 22–24 GHz 4-element CMOS phase array with on-chip coupling characterization," *IEEE J. Solid-State Circuits*, vol. 43, no. 9, pp. 2134–2143, Sep. 2008.

[31] A. Mazzanti, M. Sosio, M. Repossi, and F. Svelto, "A 24 GHz sub-harmonic receiver front-end with integrated multi-phase LO generation in 65 nm CMOS," in *IEEE Int. Solid-State Circuits Conf.*, 2008, pp. 216–608.

[32] R. M. Kodkani and L. E. Larson, "A 24-GHz CMOS passive sub-harmonic mixer/downconverter for zero-IF applications," *IEEE Trans. Microw. Theory Techn.*, vol. 56, no. 5, pp. 1247–1256, May 2008.

[33] Y.-H. Chen, H.-H. Hsieh, and L.-H. Lu, "A 24-GHz receiver frontend with an LO signal generator in 0.18-μm CMOS," *IEEE Trans. Microw. Theory Techn.*, vol. 56, no. 5, pp. 1043–1051, May 2008.

[34] V. Jain, F. Tzeng, L. Zhou, and P. Heydari, "A single-chip dual-band 22–29-GHz/77–81-GHz BiCMOS transceiver for automotive radars," *IEEE J. Solid-State Circuits*, vol. 44, no. 12, pp. 3469–3485, Dec. 2009.

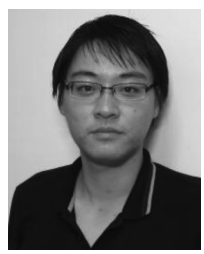

Chun-Hsing Li (S'10) received the B.S. degree in electrophysics and M.S. degree in electronics engineering from National Chiao Tung University (NCTU), Hsinchu, Taiwan, in 2005 and 2007, respectively, and is currently working toward the Ph.D. degree at NCTU.

After one year of military service as a Second Lieutenant with the Marine Corps, he was a Research Assistant with the RF System Integration Laboratory, NCTU, until June 2009. In Fall 2009, he joined the Department of Electrical Engineering, University of California at Los Angeles (UCLA). In Winter 2010, he was with the Department of Electrical and Computer Engineering, University of California at Santa Barbara. Since April 2010, he has been with NCTU. His current research is focused on RF and terahertz circuit design.

Mr. Li was a corecipient of the Best Paper Award of the 13th IEEE International Conference on Electronics, Circuits, and Systems, Nice, France, 2006. He was also the recipient of the 2011 MediaTek Inc. Fellowship.

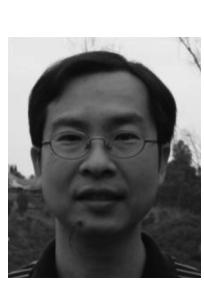

Chien-Nan Kuo (S'93–M'97) received the B.S. degree in electronic engineering from National Chiao Tung University, Hsinchu, Taiwan, in 1988, the M.S. degree in electrical engineering from National Taiwan University, Taipei, Taiwan, in 1990, and the Ph.D. degree in electrical engineering from the University of California at Los Angeles (UCLA), in 1997.

In 1997, he joined ADC Telecommunications, San Diego, CA, as a Member of Technical Staff with the Mobile System Division, where he was involved in wireless base-station design. In 1999, he joined Broadband Innovations Inc. In 2001, he joined the Microelectronics Division, IBM. He is currently an

Associate Professor with the Department of Electronics Engineering, National Chiao Tung University. His research interests include reconfigurable RF circuit and system integration design, low-power design for the application of wireless sensor networks, and development of circuit-package co-design in the system-in-package (SiP) technique.

Dr. Kuo has been a Program Committee member of the IEEE Asian Solid-State Circuits Conference since 2005 and of the IEEE Silicon Monolithic Integrated Circuits in RF Systems Conference since 2007. He was a recipient of the IEEE Graduate Fellowship Award in 1996. He was a corecipient of the 2006 Best Paper Award presented at the 13th IEEE International Conference on Electronics, Circuits, and Systems.

Ming-Ching Kuo (S'07–M'09) received the B.S. degree in electrical engineering and M.S. degree from the Institute of Electronics Engineering, National Tsing-Hua University, Hsinchu, Taiwan, in 1998 and 2000, respectively, and the Ph.D. degree in electronics engineering from National Chiao Tung University, Hsinchu, Taiwan, in 2010.

In 2001, he joined the System-on-Chip (SoC) Technology Center (STC), Industrial Technology Research Institute (ITRI), Hsinchu, Taiwan, where he contributed to transceiver design for WiFi and Mobile TV applications. In 2011, he joined MediaTek Inc., Hsinchu, Taiwan, as a Technical Manager. He is currently a Manager with the Information and Communications Research Laboratories (ICL), ITRI. His research interests include RF circuit and system integration designs, analog front-end design for medical imaging applications, and development of single photon avalanche diode (SPAD)-based sensors.